CAD-Based Calibration and Shape Measurement with StereoDIC Principle and Application on Test and Industrial Parts

Benoît Beaubier, John-Eric Dufour, François Hild, Stéphane Roux, Sylvain Lavernhe, Karine Lavernhe Taillard

To cite this version:

Benoît Beaubier, John-Eric Dufour, François Hild, Stéphane Roux, Sylvain Lavernhe, et al.. CAD-Based Calibration and Shape Measurement with StereoDIC Principle and Application on Test and Industrial Parts. Experimental Mechanics, 2014, 54 (3), pp.329-341. 10.1007/s11340-013-9794-6 . hal-00974363

HAL Id: hal-00974363
https://hal.science/hal-00974363v1

Submitted on 6 Apr 2014

Experimental Mechanics manuscript No.
(will be inserted by the editor)

CAD-Based Calibration and Shape Measurement with StereoDIC

Principle and Application on Test and Industrial Parts

Benoît Beaubier · John-Eric Dufour · François Hild · Stéphane Roux · Sylvain Lavernhe · Karine Lavernhe-Taillard

Received: date / Accepted: date

Abstract A new calibration procedure is proposed for a stereovision setup. It uses the object of interest as the calibration target, provided the observed surface has a known definition (*e.g.,* its CAD model). In a first step, the transformation matrices needed for the calibration of the setup are determined assuming that the object conforms to its CAD model. Then the 3D shape of the surface of interest is evaluated by deforming the *a priori* given freeform surface. These two steps are performed via an integrated approach to stereoDIC. The measured 3D shape of a machined Bézier patch is validated against data obtained by a coordinate measuring machine. The feasibility of the calibration method's application to large surfaces is shown with the analysis of a 2-m^2 automotive roof panel.

B. Beaubier, J.-E. Dufour, F. Hild*, S. Roux, K. Lavernhe-Taillard
LMT-Cachan, ENS Cachan / CNRS / UPMC / PRES UniverSud Paris, 61 avenue du Président Wilson
F-94235 Cachan Cedex, France
*Corresponding author: hild@lmt.ens-cachan.fr

B. Beaubier
PSA Peugeot Citroën, Centre Technique de Vélizy B, Zone aéronautique Louis Bréguet
F-78140 Vélizy Villacoublay, France

S. Lavernhe
LURPA, ENS Cachan / Univ. Paris-Sud / PRES UniverSud
61 avenue du Président Wilson, F-94235 Cachan Cedex, France

Keywords Calibration · DIC · freeform surfaces · photogrammetry · stereocorrelation

1 Introduction

The measurement of the 3D shape of large structures in industry is key to guaranteeing easy assembly and compliance with shape design, and in turn to sustaining the expected service loads. Contactless measurements are the most adapted method for the geometrical control of a complete structure (*e.g.,* plane fuselage, automotive body-in-white), or to monitor the fabrication process. Various methods exist to perform such 3D metrology. For example, Coordinate Measuring Machines (CMMs) allow the 3D shape to be measured with mechanical or optical probes. Contactless methods such as fringe projection, laser tracker or laser scanner, photogrammetry or stereovision are alternative routes. For the latter, a calibration procedure is required, but availability of a geometrical gauge shape (also called “calibration target” in the following) becomes more and more problematic as the object size gets larger. The aim of the present study is to develop a calibration method that does not involve any other calibration target but the object itself, without compromising the final uncertainty level.

StereoDIC (or 3D surface DIC) is a measurement technique of 3D shapes and surface displacement fields by registering at least two reference and two deformed pictures [1–3]. With a random pattern usually deposited onto the observed part it is possible to reconstruct the 3D shape, its deformations during a mechanical load, and to determine the in-plane strains. The method is based on stereovision principles. Clouds of 3D points are determined from at least a pair of images shot from two (or more) view points. The 3D shape is reconstructed after the calibration procedure, which consists of determining the intrinsic parameters (*i.e.,* internal parameters of cameras) and the extrinsic parameters (angle and position of the cameras in the experimental frame). Various applications of this technique have been performed at various scales [4–7].

Different ways have been proposed to determine the calibration parameters [8], which can be classified in two categories. The first one, used by Faugeras and Toscani [9], is a linearized approach to the problem. The minimization of a quadratic functional is carried out to determine the parameters using classical inversion methods (*e.g.,* pseudoinverse method [9] or singular value decomposition [10]). The difficulty with this method is that the optical distortions are not included. The second method, used by Weng *et al.* [11] or Zhang [12], consists of a two-step nonlinear optimization. A first linearization yields an initial estimate of the sought parameters. Next, an iterative method (*e.g.,* Levenberg-Marquardt) is implemented to obtain an optimal evaluation of intrinsic and extrinsic parameters. This method allows optical distortions to be included. In the work of Arfaoui and Plante [13], distortions are expressed with cubic splines, whereas Weng *et al.* [11] use parametric models.

Most of the calibration methods are based on the knowledge of a reference target geometry. These targets usually contain particular points (*e.g.,* intersection of vertical and horizontal lines, or of center of elliptical spots) which can be easily identified. The extraction of their precise location based on methods such as Peuchot's pixel detector [14] or corner detection method or center detection method [15,16] can be performed with an uncertainty of about 1/10th of a pixel. In turn, they give access to the determination of the extrinsic and intrinsic parameters. Alternatively, other works use stereocorrelation to find these parameters [17], it is also the case of the procedure presented herein.

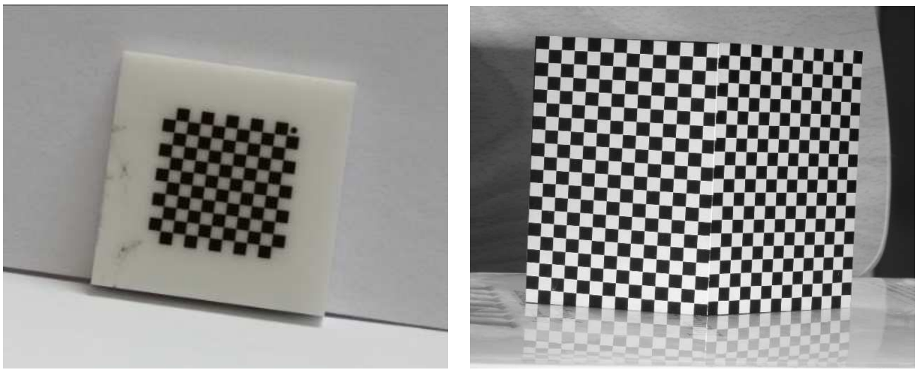

(a) Planar target [24] (b) Open book target [25]

Fig. 1 Examples of calibration targets used to determine the extrinsic and intrinsic parameters of a multi-camera stereovision system

Two different types of calibration targets are used, namely planar and 3D shapes as shown in Figure 1. To calibrate a stereosystem with the first one [2, 18, 19], many pairs (*i.e.,* 10 or more) of pictures are acquired with various positions and angles of the target (Figure 1(a)). This method has become the standard procedure in commercial software [20–24]. For 3D targets (Figure 1(b)), only one pair of pictures is required to take into account out-of-plane data. However the size of the object has to be close to that of the observed part [25, 26] if only one pair is considered. Furthermore, uncertainties are usually higher than those associated with the previous method because of the limited redundancy of the exploited data. This problem may be overcome by using several pairs of pictures. The quality of calibration is usually limited by the metrology of the calibration targets (and to a lesser degree, the uncertainty due to the point extraction). Any minute geometrical error on the target will directly affect the calibration. In the case of large structures, it is more difficult (and expensive) to ensure the geometrical quality of the calibration target.

An alternative route is to resort to self-calibration methods, which allow stereovision systems to be calibrated without the use of an additional calibration object [27]. Self-calibration consists of finding intrinsic and extrinsic parameters of the cameras directly from the pictures of the object of interest *itself*. The equations relating intrinsic parameters of the camera to the epipolar geometry have to be solved (*i.e.,* so-called Kruppa's equations [28,29]). Although very appealing, this self-calibration approach calls for many parameters to be determined from a limited information [12], and it often suffers from large uncertainties.

The aim of the present paper is to introduce a new calibration method with its possible application to industrial parts. The first novelty is related to the description of the observed surface. Contrary to standard stereoDIC procedures in which clouds of 3D points are extracted [2, 20–24, 30], the present approach explicitly deals with a continuous description of the observed surface based upon a freeform framework [31]. In that sense, it can be referred to as a global approach to stereoDIC, in the spirit of global approaches introduced in 2D-DIC and DVC [3,32,33]. Furthermore, this method is an extension of the approach proposed by Besnard *et al.* [25] in which the surface of interest and the calibration targets were observed at the same time. In the present case, the surface of interest becomes the calibration target and there is no need for using additional objects. The second novelty is related to the extraction of the calibration parameters and surface shape. Both are performed by resorting to an integrated approach to DIC [3].

The outline of the paper is as follows. First, the new approach is presented with a freeform description of surfaces, and some advantages of such a method. Then, the mathematical principle is introduced. Finally, results on test and industrial parts are discussed. An independent measurement (with a coordinate measuring machine) allows for a detailed comparison with the proposed approach. This comparison reveals reduced gaps with respect to the virtual model, decreased operating time and a significantly lower cost. The 3D shape of a large industrial part is also analyzed and its change during welding.

2 Surface Representation with NURBS

To address the challenges of the study, namely, the large size of the observed part, and the difficulties of making a large calibration target, a new calibration methodology is developed based upon *a priori* knowledge of the 3D geometry of the observed surface. It thus departs from standard self-calibration techniques [27]. In the first step of the calibration, the observed object is considered to comply exactly with the theoretical description of its geometry, here a freeform surface description (using Non-Uniform Rational Basis Spline or NURBS patches [31]). This type of model is very common since nowadays most studied parts have a CAD representation [31, 34].

Let us introduce NURBS [31], which is the chosen modeling of the shape of interest. NURBS are a mathematical model for representing freeform surfaces. It is the elementary basis used in CAD software [31,34]. A NURBS patch is defined by its order, a network of control points with associated weights, and its knot vector (Figure 2).

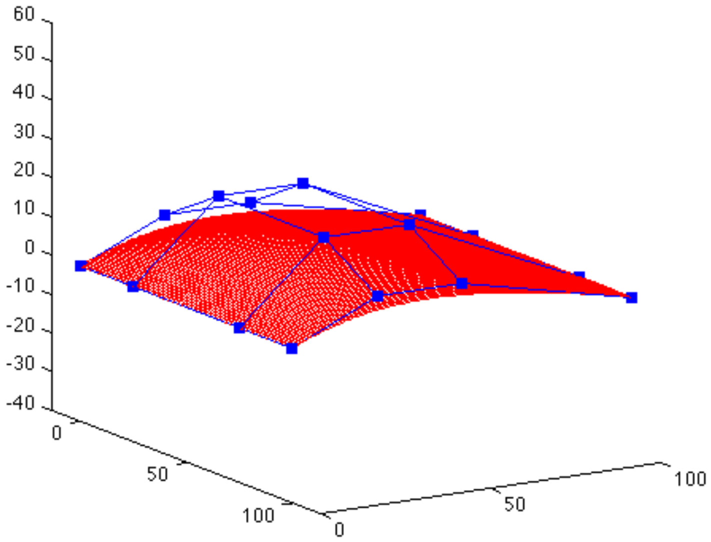

Fig. 2 Theoretical NURBS patch. The blue squares define the control points and the red surface is the 3D shape of interest. Dimensions are in millimeters

Table 1 Key features of different 3D shape measurement methods (evaluated by the authors)

Measurement solution	Contactless			CMM
Calibration target	planar target [20–24]	open book target [25]	**object (this work)**	spheres
D.O.F.	$\approx 60,000$	$\approx 60,000$	**48**	$4,680$
Measurement time	1 h	3 h	**2 h**	4 h
Image pair	at least 10	at least 1	**1**^{b}	none
Surface description	3D point cloud	3D point cloud	**Freeform surface**	3D point cloud

^{b}Only one pair can be used provided the object is not planar or quasi planar.

The surface $\boldsymbol{X}(u,v)=(X,Y,Z)$ is defined in the parametric space (u,v) as

$$\boldsymbol{X}(u,v)=\frac{\sum_{i=0}^{m}\sum_{j=0}^{n}N_{i,p}(u)N_{j,q}(v)\omega_{ij}\boldsymbol{P_{ij}}}{\sum_{i=0}^{m}\sum_{j=0}^{n}N_{i,p}(u)N_{j,q}(v)\omega_{ij}} \tag{1}$$

with

$$\forall u\in[0,1], N_{i,0}(u)=\begin{cases}1 \text{ when } u_i\leq u\leq u_{i+1}\\ 0 \text{ otherwise}\end{cases} \tag{2}$$

and

$$N_{i,p}(u)=\frac{u-u_i}{u_{i+p}-u_i}N_{i,p-1}(u)+\frac{u_{i+p+1}-u}{u_{i+p+1}-u_{i+1}}N_{i+1,p-1}(u) \tag{3}$$

where $N_{i,p}$ are mixing functions, $\boldsymbol{P_{ij}}=(X_{Pij},Y_{Pij},Z_{Pij})$ are the coordinates of control points of the surface, ω_{ij} corresponding weights, $(m\times n)$ the number of control points and (p,q) the degrees of the surface. This formalism has many advantages, including that it is relatively simple to implement numerically, and it is already used by any CAD software, particularly in step format. Figure 2 shows the NURBS model of the tested part used in this study, in red, the theoretical surface $\boldsymbol{X}(u,v)$ and in blue the corresponding control polygon $\boldsymbol{P_{ij}}$ of the NURBS patch.

Furthermore, a calibration target is not necessary since the observed surface *itself* can be used. The practical implementation is easier and faster. The calibration is performed with the first pictures of the series to be analyzed during, say, a mechanical test. The choice of freeform surface descriptions enables the number of parameters required to model the shape to be drastically reduced. Tens of parameters are needed to describe a simple geometry with a freeform surface, whereas, there are thousands of degrees of freedom in a point cloud (Table 1). The normal to the surface, which is of paramount importance to evaluate strains, can be computed at any point without any additional post-processing. Last, the metrological characterization of the observed surface will be directly expressed in the language of description of the CAD model. Therefore, there is no need to reproject or interpolate the measurements since they are expressed in the relevant basis.

3 CAD-Based Calibration and 3D Shape Measurement

The classic camera model is a projection, and results from three simple geometric transformations [9]. The first transformation expresses the 3D coordinates of a point of the observed surface in the camera reference frame. This transformation is described by a matrix by, for instance, using homogeneous coordinates with a rotation and a translation, and the parameters of this matrix are the extrinsic parameters. The second is the perspective projection of this point in the retinal plan. This transformation reveals the scale factors. The third expresses the latter in the picture reference frame. This is an affine transformation composed of four parameters, namely the intrinsics parameters. In the following, all these extrinsic and intrinsic quantities are collectively called the calibration parameters.

In the present case, two main quantities have to be determined, namely, the transformation matrices (as in any stereoDIC algorithm) or equivalently the extrinsic and intrinsic parameters, and the actual metrology of the observed surface as only its *theoretical* definition (*i.e.,* its CAD model) is known. The two-step calibration procedure introduced hereafter is non standard. The observed surface is therefore the calibration target.

3.1 Transformation Matrices

The relationships between 3D points (of coordinate $\boldsymbol{X} = (X, Y, Z)$) in the frame of the observed part and their projections onto left and right pictures (of coordinates (x^l, y^l) and (x^r, y^r), respectively) are given by

$$\left\{\begin{matrix} s^l x^l \\ s^l y^l \\ s^l \end{matrix}\right\} = [\boldsymbol{M}^l]\{\overline{\boldsymbol{X}}\} \quad \text{and} \quad \left\{\begin{matrix} s^r x^r \\ s^r y^r \\ s^r \end{matrix}\right\} = [\boldsymbol{M}^r]\{\overline{\boldsymbol{X}}\} \tag{4}$$

where s^l and s^r are scale factors, and $\{\overline{\boldsymbol{X}}\} = (X, Y, Z, 1)^t$ are the corresponding homogeneous coordinates of any 3D point [9, 25].

By remembering that the 3D points belong to a *single* surface (*e.g.,* NURBS patch) described in the parametric space (u, v), the previous equations are rewritten as

$$\left\{\begin{aligned} x^{l,r}(u,v) &= \frac{M^{l,r}_{1i}\overline{X}_i(u,v)}{M^{l,r}_{3i}\overline{X}_i(u,v)} \\ y^{l,r}(u,v) &= \frac{M^{l,r}_{2i}\overline{X}_i(u,v)}{M^{l,r}_{3i}\overline{X}_i(u,v)} \end{aligned}\right. \tag{5}$$

where Einstein's convention is used. The problem has *a priori* 24 unknowns (*i.e.,* 24 parameters $M^{l,r}_{ij}$ of the transformation matrices $[\boldsymbol{M}^l]$ and $[\boldsymbol{M}^r]$) to be determined. They will be evaluated by resorting to a DIC-based algorithm. The pictures shot by left and right cameras are respectively denoted by $f(\boldsymbol{x}^l)$ and $g(\boldsymbol{x}^r)$, where $\boldsymbol{x}^l = (x^l, y^l)$ and $\boldsymbol{x}^r = (x^r, y^r)$. The gray level conservation requires that

$$f(\boldsymbol{x}^l) = g(\boldsymbol{x}^r) \tag{6}$$

However, this conservation only holds if the exact calibration parameters are known (*i.e.,* the two transformation matrices) and no acquisition noise is present. In practice, this is not the case, and therefore a global formulation is needed in which the sum of squared differences expressed in the parametric space

$$\mathcal{T} = \int_{\text{ROI}} [f(\boldsymbol{x}^l(u, v, M^r_{ij})) - g(\boldsymbol{x}^r(u, v, M^r_{ij}))]^2 \mathrm{d}u\mathrm{d}v \tag{7}$$

is minimized with respect to $M^{l,r}_{ij}$ over the region of interest (ROI). As in any standard global approach [3, 32], a modified Newton scheme is used to minimize the sum of squared differences. This is achieved by considering the linearized sum of squared differences

$$\mathcal{T}_{\text{lin}}(\mathrm{d}M^{l,r}_{ij}) = \int_{\text{ROI}} [f(\boldsymbol{x}^l) - g(\boldsymbol{x}^r) + (\boldsymbol{\nabla} f \cdot \delta\boldsymbol{x}^l)(\boldsymbol{x}^l) - (\boldsymbol{\nabla} g \cdot \delta\boldsymbol{x}^r)(\boldsymbol{x}^r)]^2 \mathrm{d}u\mathrm{d}v \tag{8}$$

where corrections associated with changes of the calibration parameters $\mathrm{d}M^{l,r}_{ij}$ update the left and right coordinates ($\delta\boldsymbol{x}_l$ and $\delta\boldsymbol{x}_l$) of any 3D point

$$\delta\boldsymbol{x}^{l,r} = \frac{\partial\boldsymbol{x}^{l,r}}{\partial M^{l,r}_{ij}} \mathrm{d}M^{l,r}_{ij} \tag{9}$$

In Equation (7), $\boldsymbol{x}_l$ and $\boldsymbol{x}_r$ denote the current estimates of the 2D positions of 3D points obtained with the current estimate of matrices $[\boldsymbol{M}^l]$ and $[\boldsymbol{M}^r]$. Consequently, a 'pseudo' kinematic basis is devised in Equation (9) to compute the changes of $\boldsymbol{x}_l$ and $\boldsymbol{x}_r$ with respect to $M^{l,r}_{ij}$. It corresponds to the sensitivity displacement fields to any of the considered unknown. Since the unknown parameters are a direct output of the registration, this type of analysis corresponds to an integrated DIC [3, 35] scheme. In practice, only 22 parameters are considered since both matrices are determined up to a multiplicative constant (*i.e.,* $M^{l,r}_{34}$). To address this issue, three routes can be followed. First, the ROI encompasses the whole CAD definition. In that case, either nominal distances are considered or the measurement of a least one distance is needed to get an absolute (*i.e.,* metric) estimate. Second, if special features for which an absolute distance is available (*i.e.,* nominal or actually measured), it corresponds to the same situation as before. Third, if no special feature for which an absolute distance is available, the user needs put some additional markers for which the distance is known or measured.

Furthermore, an initial guess is needed (*i.e.,* $\boldsymbol{x}^l_0 = \boldsymbol{x}^l([\boldsymbol{M}^l_0])$ and $\boldsymbol{x}^r_0 = \boldsymbol{x}^r([\boldsymbol{M}^r_0])$). This corresponds to the first step of the calibration procedure (Figure 3). At least 6 points are selected by the user on the theoretical surface $\boldsymbol{X}(u,v)$, and on the right and left pictures $(x_i^{l,r}, y_i^{l,r})$. The three-dimensional coordinates (X_i, Y_i, Z_i) are selected on the CAD model of the observed part. System (4) is solved to determine $[\boldsymbol{M}_0^r]$ and $[\boldsymbol{M}_0^l]$ via a singular value decomposition [10]. From these results, the values $M_{34}^{l,r}$ are not altered anymore.

The updated components of the transformation matrices are determined by assuming that the actual surface is described by a *known* global description (*i.e.,* its CAD model). A multiscale correlation algorithm is used as in a standard DIC procedure [3]. In contrast to classical DIC in which the reference picture does not change during the minimisation procedure, both pictures are updated at each iteration (see Equation (8)) in the present case.

3.2 Surface Metrology

The second step consists of finding the best CAD-surface by moving control points $\boldsymbol{P_{ij}}$ of the theoretical surface with *known* transformation matrices (Figure 4) to match the actual shape. Control points $(\boldsymbol{P_{ij}}$ become the new unknowns and are updated by using the same type of correlation procedure as described in Section 3.1. The main difference is given by the sensitivity displacement fields that read

$$\delta \boldsymbol{x}^{l,r} = \frac{\partial \boldsymbol{x}^{l,r}}{\partial \boldsymbol{X}} \frac{\partial \boldsymbol{X}}{\partial \boldsymbol{P_{ij}}} \mathrm{d}\boldsymbol{P_{ij}} \tag{10}$$

In the present test case, there are 48 unknowns (*i.e.,* 3 × 16 coordinates of the 16 control points of the NURBS patch). They correspond to the 48 degrees of freedom given in Table 1. This number may be considered as large, but it is to be compared with standard stereoDIC usage where 10^4 degrees of freedom or more are not uncommon for the whole region of interest.

3.3 Iterative Scheme

The two previous sections each define an iterative procedure to determine the transformation matrices and the control points of the freeform surface model of the observed part. For each of these steps, the algorithm is iterated to reach the global minimum of the correlation residuals, expressed in percent of the dynamic range of the gray level. When convergence is reached for a given step, say concerning the transformation matrices, the second step consists of a metrological characterization of the actual surface. These two steps are repeated until no more detectable change occurs neither on transformation nor on shape parameters. The outputs of this new calibration procedure are the components of the

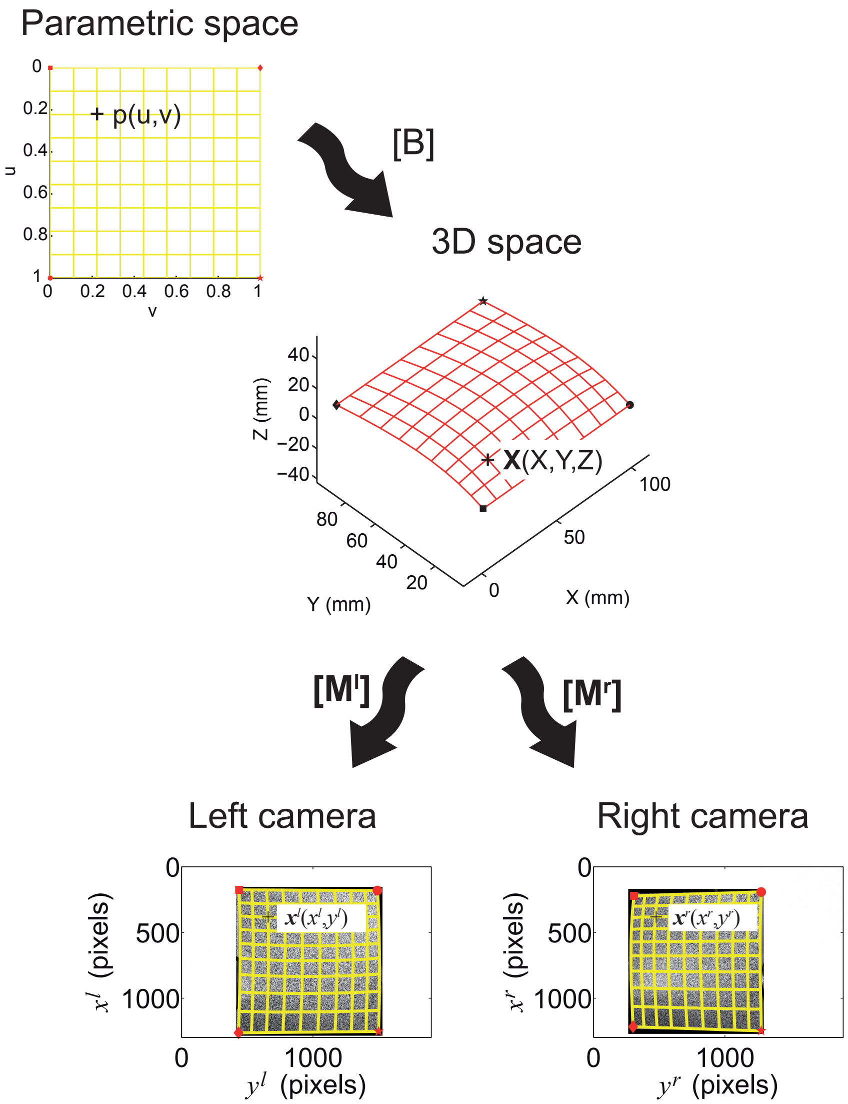

Fig. 3 Principle of the first step of the calibration procedure: the transformation matrices $[\boldsymbol{M}_0^r]$ and $[\boldsymbol{M}_0^l]$ are sought

transformation matrices and the 3D shape of the surface of interest, which plays the role of the calibration target.

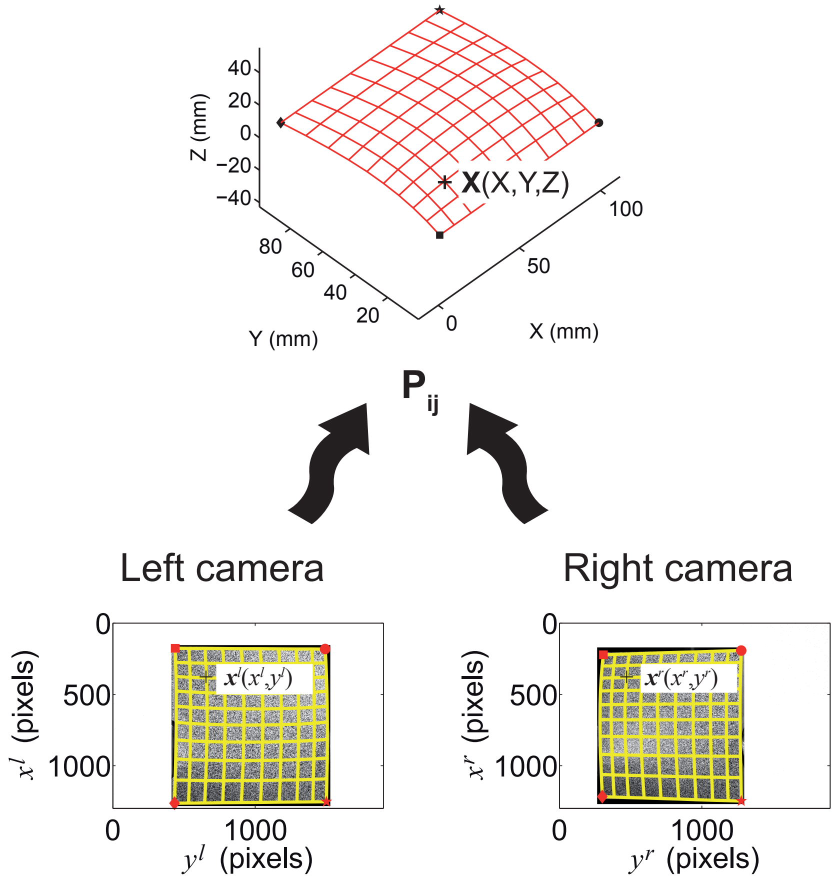

Fig. 4 Principle of the second step of the calibration procedure: the 3D shape is measured (*i.e.*, the actual position of the control points $\boldsymbol{P_{ij}}$ is sought)

4 Results and Application

In the sequel, two different applications are discussed. The first case is a machined Bézier patch and corresponds to a proof of concept of the whole procedure proposed herein. The second application deals with a 2-m^2 automotive roof prior to and after welding.

4.1 Test Part

To validate the calibration procedure a 100 × 100 mm test part made of aluminum alloy was machined (Figure 5(a)(a)). Its CAD surface was designed from a first order NURBS patch in CatiaV5 [36]. The parameters of the test part are defined in Table 2. Since all the weights are equal to one, the surface actually corresponds to a third order Bézier patch. The test part was milled on a 3-axis High Speed Machine (HSM). To minimize deviations induced by milling between the CAD model and the machined geometry, machining tolerance and scallop height are required to be less than 1 μm. A real time polynomial interpolation is also used for the numerical control (CNC) options of the HSM to minimize chordal errors and to improve the follow-up. Four 'curves' (*i.e.,* grooves) corresponding to isoparametric curves are milled on the part (Figure 5(a)). They correspond to

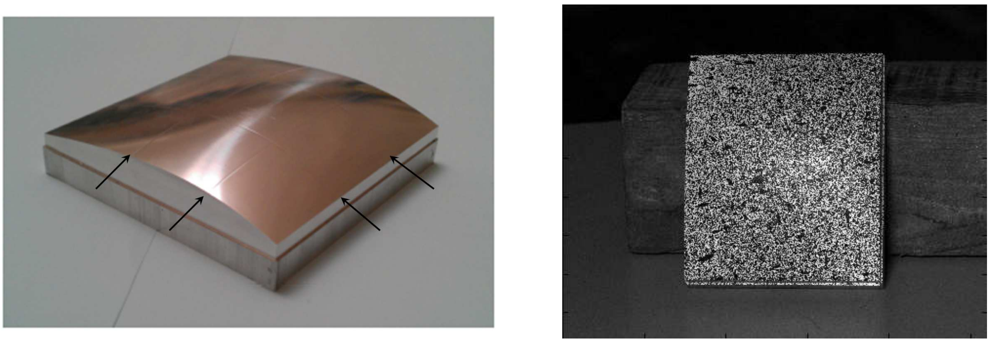

(a) Machined part made of aluminum alloy (b) Painted part with random pattern

Fig. 5 Test part consisting of a single Bézier patch. (a) Four grooves, which correspond to the isoparametric curves defined in Equation (11), are also milled. The arrows show their intersection with the sample side. (b) When covered by the speckle pattern, the grooves are no longer visible

$$\begin{cases} C_1(v) = \boldsymbol{X}(u^* = 1/3, v) \\ C_2(v) = \boldsymbol{X}(u^* = 2/3, v) \\ C_3(u) = \boldsymbol{X}(u, v^* = 1/3) \\ C_4(u) = \boldsymbol{X}(u, v^* = 2/3) \end{cases} \tag{11}$$

However, it is not possible to see the grooves with bare eyes, because they are masked by the random pattern (Figure 5(b)).

After milling, a random pattern is deposited onto the machined part (Figure 5(b)). The pictures are taken by Canon EOS 40D cameras. A LED panel is used to illuminate the scene. This lighting device allows the reflection of the light on the observed part to be minimized (although not completely avoided).

Table 2 Control points of the milled surface, dimension are in mm, and all the associated weights are equal to one; associated knot vectors are u={00001111} and v={00001111}

	P_{11}	P_{12}	P_{13}	P_{14}	P_{21}	P_{22}	P_{23}	P_{24}	P_{31}	P_{32}	P_{33}	P_{34}	P_{41}	P_{42}	P_{43}	P_{44}
X	0	0	0	0	25	25	25	25	75	75	75	75	100	100	100	100
Y	0	25	50	100	0	25	50	100	0	25	50	100	0	25	50	100
Z	0	0	0	0	10	20	20	10	10	20	20	10	0	0	0	0

4.1.1 Results

Figure 6(a) shows the correlation residuals after convergence of the first step. It consists of calculating the difference between left and right pictures at the end of the registration procedure. It is expressed in the parametric space of the 3D surface (u, v). The Root Mean Square (RMS) value of the correlation residual $|f(\boldsymbol{x}^l) = g(\boldsymbol{x}^r)|$ is $\eta = 2.0$ % of the gray level dynamic range of f (*i.e.*, $\max f - \min f$. This is a very small value so that the matching of the two pictures is deemed successful. The largest differences are due to a spurious specular reflection of light on the surface. The fact that the grooves appear on the residuals is an additional indication of the registration quality (since they cannot be seen on the textured surface, see Figure 5(b)). On this correlation residual map, some errors remain due to the gap between real and theoretical surfaces. Figure 6(b) shows that the geometry of the real shape is close to the theoretical one. Only three iterations are necessary to reach convergence. The RMS value of the correlation residual is slightly lower than in the previous step.

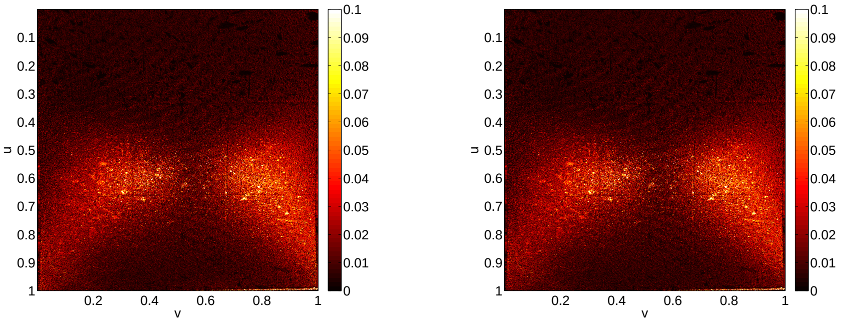

(a) First step, RMS value $\eta = 2.0$ % (b) Second step, RMS value $\eta = 1.99$ %

Fig. 6 Map of the correlation residuals expressed in percentage of the gray level dynamic range of the analyzed pictures for the two calibration steps. Note that the maps are shown in the parametric space (u, v)

4.1.2 Correction of Distortions

It is important to mention that a correction of distortions has been performed on the right and left pictures. This correction improves the results on the edges of the pictures. Distortions are evaluated with an integrated DIC approach based upon a parametric model [37]. The correction algorithm uses a global DIC method between a picture of an etched target and its numerical model. This calibration target is a steel plate where randomly generated dots have been engraved. This method differs from traditional ones [11, 38, 39] because it is not a geometrical method. It is only based on digital image correlation. In the present case, this correction method allows us to separate the distortion correction from the calibration of the stereovision setup.

Figure 7 shows the correlation residual map before taking into account the optical distortions. The main difference can be seen near the edges of the picture (*i.e.,* where the distortions are the highest). The effect of distortion correction is analyzed on the 3D reconstructed surface in the following section. In terms of the RMS value of the correlation residual, there is a clear gain to be expected from the distorsion correction.

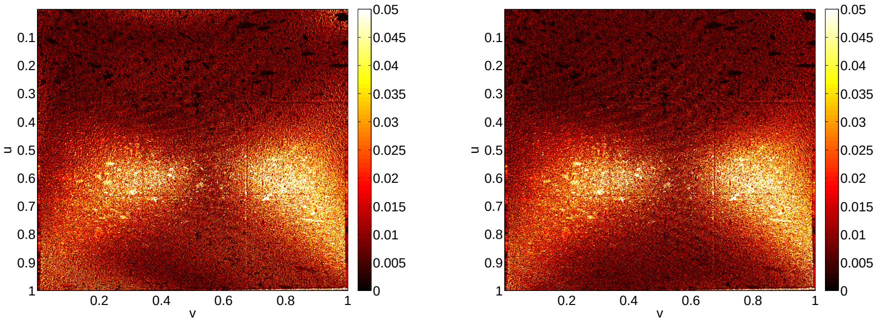

(a) Without correction, RMS value: $\eta = 2.1$ % (b) With correction, RMS value $\eta = 2.0$ %

Fig. 7 Comparison between the residual map expressed in percentage of the gray level dynamic range of the analyzed pictures without correction of distortions (a) and with correction of distortions (b) at the end of the first calibration step

4.1.3 Comparison with CMM Measurements

A comparison is performed between the measurement of the tested surface with CMM taken as a reference, and by the stereoDIC approach developed herein. The measurement has been carried out on an automated machine. The calibration procedure of the CMM has shown that the repeatability was about 0.4 μm and the shape error on the calibration sphere was about 0.7 μm. The setup of the global frame was performed by probing some items that constitute a frame {plane-line-point}. The CMM table was taken as the reference plane. The intersection of the two side surfaces probed on the milled part was the line, and the point was the intersection of the plane and the line. A total of $39 \times 40 = 1560$ points were measured on the part (Figure 8(a)). The center of the probing sphere was extracted for each point. A post-processing operation was necessary to calculate the surface points (Figure 8(b)). The actual contact point was computed thereafter from the position of the probing sphere and the normal to the surface. The gap between the model and the computed contact point was determined by minimization. Last the optimal repositioning of the shape was obtained resorting to a Newton-Raphson method. All these operations are iterated up to convergence.

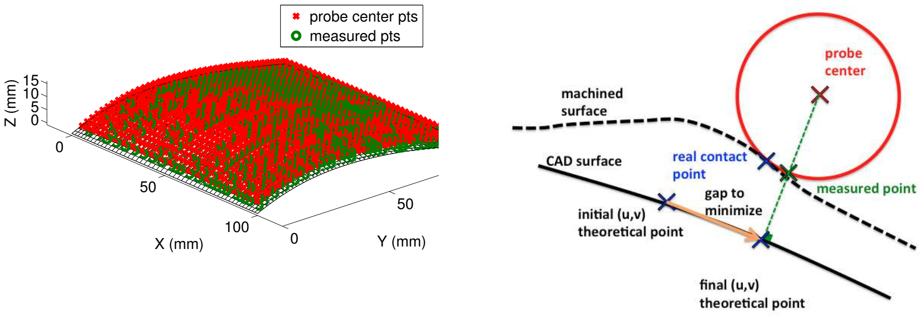

(a) Probe and measured points

(b) Construction of measured point

Fig. 8 Freeform surface reconstruction from a scatter plot obtained by CMM. (a) The probe locations are defined by red crosses and reconstructed points by green circles. The reconstructed surface is in black. (b) Contact point computed from a probe point, the real contact point is in blue and the calculated contact point is in green

Gap measurements from CAD-based stereoDIC are performed with the same calculation method. However, setup and projection steps are useless because the real shape directly results from the correlation algorithm in the frame of the reference surface. For each point N belonging to the measured shape, it consists of finding point M of the reference surface that minimizes the distance between M and N. This procedure is repeated for any point of interest. Figure 9 shows the gap map between the theoretical and the real shapes when measured by CMM (Figure 9(a)) and by CAD-based stereoDIC (Figure 9(b)). The RMS difference is 11.4 μm for the CMM measurement with respect to the virtual model, and 5.7 μm for the CAD-based stereoDIC measurement. The number of degrees of freedom is also lower for CAD-based stereoDIC than for CMM measurements, and the CMM result being a 3D point cloud, it is by construction noisier than CAD-based stereoDIC, which explains a part of the RMS difference. Moreover, uncertainties on CMM measurements can reach $4-5$ μm because of the projection [40], which also explains the differences observed. Moreover, Table 1 shows that the measurement time is 4 hours for the CMM measurement and 2 hours with the present approach. Furthermore, concerning CAD-based stereoDIC, the complete measurement time mainly depends on the computation time. Improvement of the implementation and/or change of computer will easily decrease this time. On the contrary, the measurement time of CMMs is limited by the machine *itself*. Last, the object size is not a limitation for CAD-based stereoDIC since only a computer and two cameras are needed. In case of CMM, large scale CMMs allow such objects to be measured but it is much more expensive.

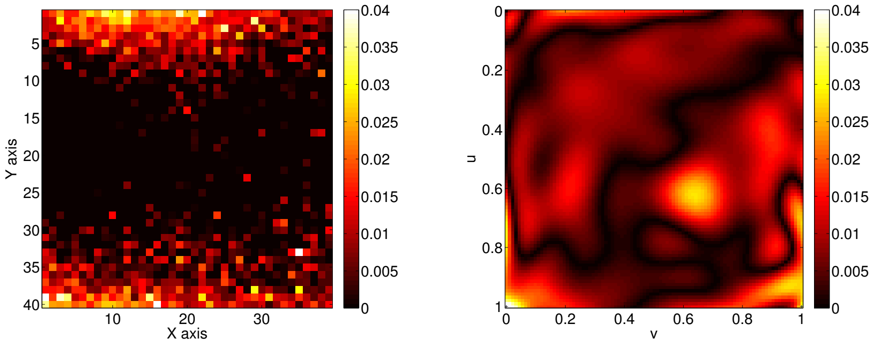

(a) CMM data (b) CAD-based stereoDIC

Fig. 9 Comparison of differences between CMM and CAD-based stereoDIC with respect to the virtual CAD model of the patch. Gap values are in mm. Note that the CMM 'frame' is associated with the point numbering, and the parametric space for CAD-based stereoDIC

Figure 10 shows the importance of the correction for optical distortions on the result. The measured gap before taking into account the correction is farther away from the theoretical model, in particular on the edges of the picture. The RMS gap is of 5.7 μm for the stereoDIC measurement with the optical distortions correction and 21 μm without. There is a clear (*i.e.*, $\approx$ fourfold) gain when optical distortions are accounted for.

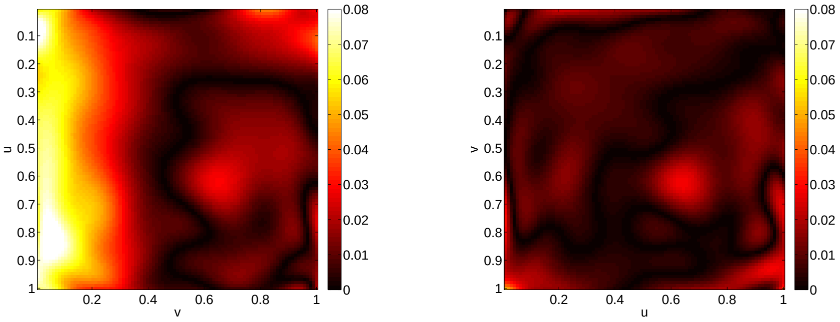

(a) No correction

(b) With corrections

Fig. 10 Comparison between the gap map without (a) or (with) correction of distortions. Note that the same color-bar is used in both maps

4.2 Application to Large Scale Industrial Part: Automotive Roof

CAD-based stereoDIC is applied to an industrial part. The considered geometry is an automotive roof made by PSA Peugeot-Citroën, whose external surface area is about 2 m^2 (Figure 11). The aim is to determine the deformation of 3D shape induced by the assembly process, here a welding brazing operation. The CAD-based stereoDIC procedure is the same as for the test part, with the difference that the measurement is carried out online (*i.e.*, on a manufacturing cell of an automated assembly line). This cell is composed of two welding brazing robots (to assemble both sides at the same time) and a conveyor on which the body shell is positioned.

The stereovision setup consists of two 12-Mpixel Teli CleverDragon® cameras located about two meters above the observed part and equipped with 24-mm Nikkor (from Nikon) lenses. The acquisition frequency is about 10 Hz, , which is high enough compared with the velocity of the welding brazing head (*i.e.*, 30 mm/s), and the integration time is of the order of 10 μs. The definition of the pictures is about 3000 × 4000 pixels. Hence, the physical size of the pixel is of the order of 0.3 mm. Such a resolution is necessary for this application. The scene is lit by two light spots on both sides of the body shell.

The difficulty is to limit the light reflection on the roof. To address this point, a grazing lighting was chosen. Yet the result is not completely satisfactory. However, it is believed with the global DIC approach it has a minimal effect on the reconstructed 3D shape. Some additional investigation will be needed to prove this statement. The velocity of welding brazing process being of 25 mm/s, the duration of the test is about 60 s. The analysis of the 3D deformation is carried out using a random pattern deposited onto the entire roof as shown in Figure 11.

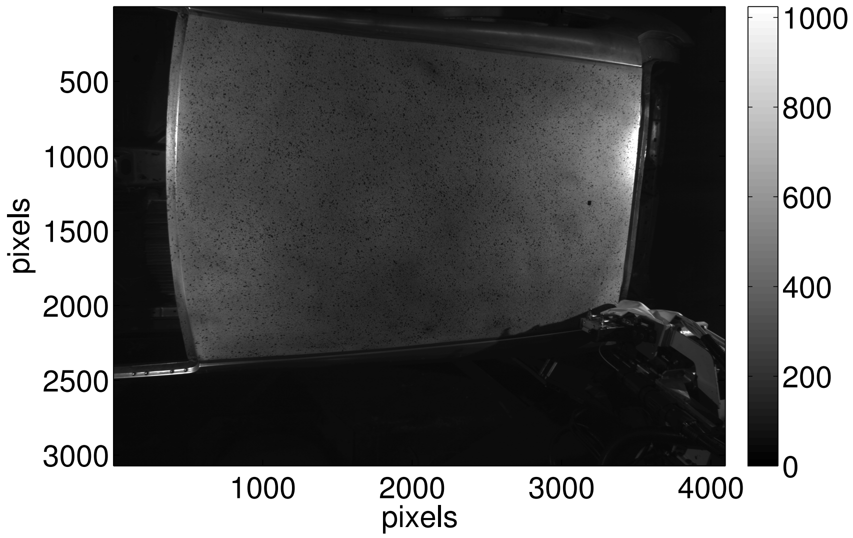

Fig. 11 Picture of the roof (2 m^2 surface area) taken by the left camera

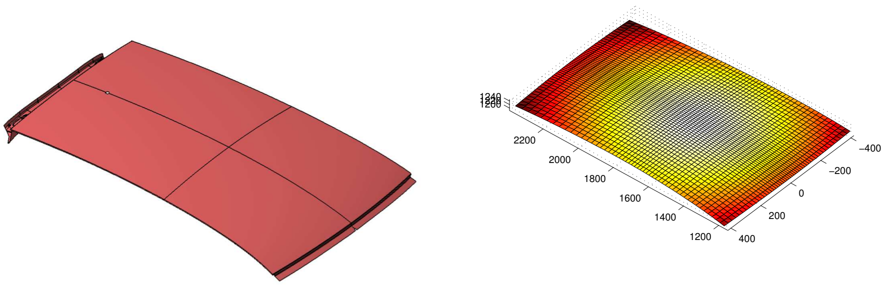

(a) Initial CAD model of the Citroën C4 roof (b) Extracted NURBS patch

Fig. 12 Virtual CAD models of the observed roof (see Figure 11)

The CAD model shown in Figure 12(a) is taken as a reference for the stereo-correlation procedure. To work with this geometry, a simplification step is necessary. All the useless elements of the geometry, such as the gutter on the side of the roof are removed. Figure 12(b) shows the geometry after the extraction step. This shape is made up of only one NURBS patch. It is composed of $12 \times 7 = 84$ control points with unitary weight. Thus it corresponds to an 11×6 order Bézier patch.

4.2.1 Initial and Final Shapes

The calibration procedure is carried out on the post welded shape of the roof. It provides the transformation matrices and the final 3D shape of the roof. This choice is made since the CAD model is based on the final shape of the assembled body in white. The final shape is expected to be closer to its CAD definition. For the initial shape of the roof (*i.e.,* the pre welded part), the same calibration parameters are used and only the second step of the calibration procedure is run (*i.e.,* the control points are moved to match as best as possible the initial shape of the roof). Figure 13(a) shows the map of correlation residuals for the geometry of the roof before assembly. The region to be welded is on the left of the picture, and the back of the roof is at the bottom (the hole for the antenna attachment can be seen in yellow when $u = 1, v \approx 0.5$). The result is satisfactory. The maximum error is at the bottom of the map. The RMS level is of the same order of magnitude as before (*i.e.,* about 2.2 %). The black area around the center of Figure 13(a)(a) is believed to be due to illumination artifacts.

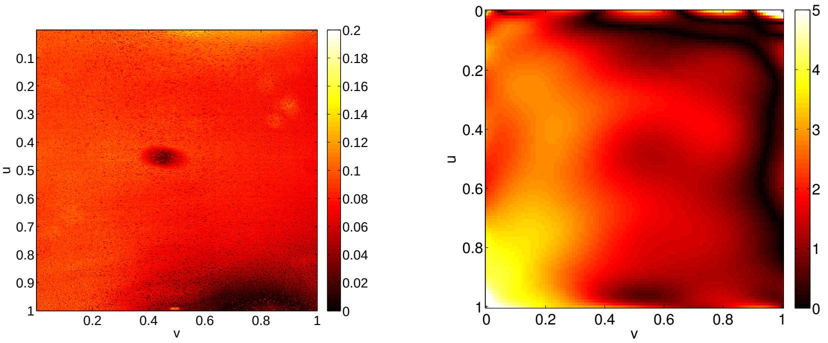

Fig. 13 Results for the roof placed on the body shell but not welded. Map of the absolute correlation residuals, expressed in percent of the dynamic range of the analyzed pictures (a). Gap between the theoretical shape and the measured surface. Gap values are in mm

After welding brazing, the correlation residuals are almost identical to the previous ones (Figure 14(a)). The registration quality is the same in both cases. Comparing the initial (Figure 13(b)) and final (Figure 14(b)) gaps of the measured 3D surface with its theoretical description, it is concluded that the welded shape is closer to the theoretical model. As for the initial configuration, convergence of the algorithm is reached very quickly and the correlation residuals are small (RMS residual for the pre welded roof: 2.2%, and for post welded roof: 2.3%), showing that the initial guess (the CAD model of the surface) is very close to the real shape of interest.

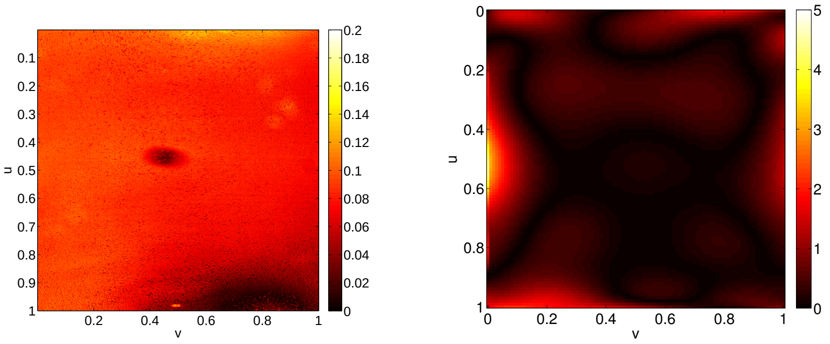

Fig. 14 Results for the roof welded on the body shell. Map of the absolute correlation residuals, expressed in percent of the dynamic range of the analyzed pictures (a). Gap between the theoretical shape and the measured surface. Gap values are in mm

4.2.2 CAD Metrology of Roof

After these operations it is possible to evaluate the impact of the welding-brazing process onto the geometry of the roof. Figure 15 represents the gap between the geometry of the roof before and after the welding brazing process. This map shows that the roof has undergone a displacement norm of about 6 mm in the welding brazed zone (on the left of the picture). This is to be expected because of the pressure system used to conform the shape. The impacted zone by welding brazing is relatively wide. However, there is no real impact of the welding brazing on the opposite side (right side). Hot "spots" near the upper right corner are areas where the gap estimation has not converged (*i.e.*, the convergence criterion is not reached). Last, the gap between the CAD model and the welded part has been reduced from its initial value. This constitutes a validation of the welding process.

5 Conclusion

A new method of stereovision system calibration is developed. It is based on the use of the CAD model of the observed part as an initial guess of the registration algorithm. Consequently, no calibration target is needed. It belongs to the class of self-calibration techniques. This method allows for the use of the object of interest as a calibration by itself, thus rendering the stereovision system much more flexible, easy and quick without compromising the quality of the measurements. The two-step calibration is performed by resorting to integrated stereoDIC to determine the components of the transformation matrix and the

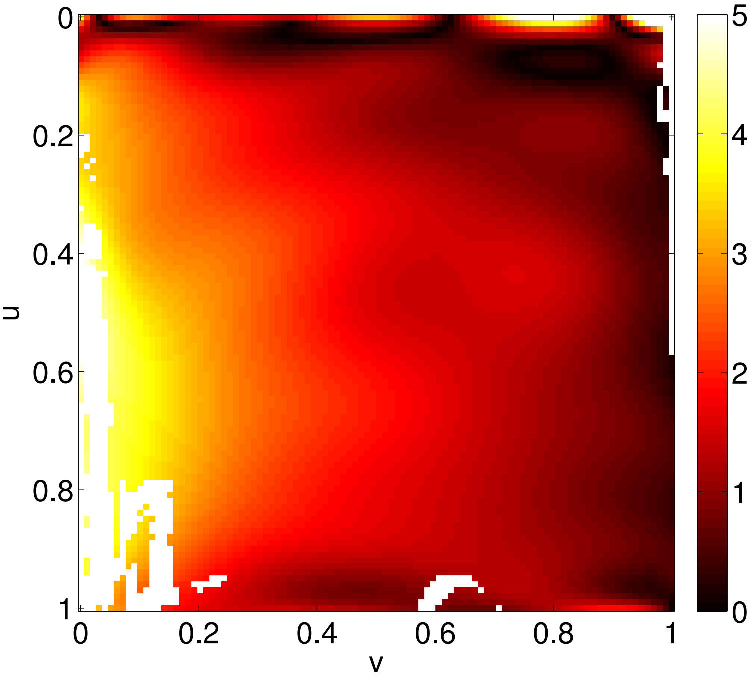

Fig. 15 Deformation the roof after welding brazing. The reference is the pre welded roof geometry, values of the norm of the gap are in mm

actual shape of the observed surface in the language of freeform surfaces (*i.e.*, NURBS in the present case).

The result of the method has been validated by comparison with a CMM measurement on a machined third order Bézier patch. The gap between the measured and theoretical shapes was lower for the present approach than that found for CMM measurements. Part of this difference is due to the need for performing frame setup with CMM and any stereoDIC procedure yielding 3D point clouds. To proceed along this path, the evaluation of the uncertainty levels is needed to evaluate the quality of the 3D reconstruction.

The feasibility of the method to deal with large parts has been shown by following *in situ* the welding process of a 2-m^2 automotive roof. In particular, it is shown that after the process, the shape is closer to its theoretical description than the initial (*i.e.*, unwelded) roof. In both analyzed examples, rather simple NURBS patches were used. More complex shapes will be studied in the future. The results presented herein constitute a proof of concept of CAD-based stereoDIC. Some additional developments are needed. The first one corresponds to the measurement of 3D displacements. In the present case, the deformation during welding was measured by the comparison of 2 NURBS surfaces. Another way of performing this operation is to explicitly move the control points of the measured surface to evaluate the 3D displacements.

The choice of freeform surface descriptions is logical for a global approach to stereocorrelation since it is used when designing various parts. It becomes even more interesting since isogeometric analyses are currently being developed to bridge the gap between CAD and finite element methods (FEM) [34]. By construction, the present development is a dense multiview method [41]. It is worth noting that other approaches are based upon the use of facets, say by resorting to Delaunay triangulation [42]. This type of discretization may also be performed in the present framework.

Acknowledgements This work was partly supported by PSA Peugeot-Citroën, and by a grant from Région Île de France.

References

1. Helm JD, McNeill SR, Sutton MA (1996) Improved three-dimensional image correlation for surface displacement measurement. Opt. Eng. 35:1911-1920
2. Sutton MA, Orteu J-J, Schreier H (2009) Image correlation for shape, motion and deformation measurements: Basic Concepts, Theory and Applications. Springer, New York, NY (USA)
3. Hild F, Roux S (2012) Digital Image Correlation. In: Rastogi P, Hack E (eds) Optical Methods for Solid Mechanics. A Full-Field Approach. Wiley-VCH, Weinheim (Germany)
4. Sutton MA, Li N, Garcia D, Cornille N, Orteu JJ, McNeill SR, Schreier HW, Li X, Reynolds AP (2007) Scanning Electron Microscopy for Quantitative Small and Large Deformation Measurements Part II: Experimental Validation for Magnifications from 200 to 10,000. Exp. Mech. 47:789-804
5. Orteu JJ (2009) 3-D computer vision in experimental mechanics. Optics Lasers Eng. 47:282-291
6. Lei Z, Kang HT, Reyes G (2010) Full field strain measurement of resistant spot welds using 3D image correlation. Exp. Mech. 50:111-116
7. Pottier T, Vacher P, Toussaint F, Louche H, Coudert T (2012) Out-of-plane Testing Procedure for Inverse Identification Purpose: Application in Sheet Metal Plasticity. Exp. Mech. 52:951-963
8. Salvi J, Armague X, Battle J (2002) A comparative review of camera calibrating methods with accuracy evaluation. Pattern Recog. 35:1617-1635
9. Faugeras O, Toscani G (1987), Camera calibration for 3D computer Vision. International Workshop on Machine Vision and Machine Intelligence 240-247.
10. Morvan Y (2009) Acquisition, compression and rendering of depth and texture for multi-view video. PhD thesis, Eindhoven University of Technology
11. Weng J, Cohen P, Herniou M (1992) Camera calibration with distortion models and accuracy evaluation. IEEE Trans. Pattern Anal. Machine Intell. 14:965-980

12. Zhang Z (2000) A flexible new technique for camera calibration. IEEE Trans. Pattern Anal. Machine Intell. 22:1330-1334
13. Arfaoui A, Plante F (2011) Camera Calibration Using Composed Cubic Splines. http://lrio.copl.ulaval.ca/PDF/2011_Arfaoui_Plante_Camera Calibration Using Composed Cubic Splines_Final.pdf
14. Peuchot B (1993) Camera Virtual Equivalent Model 0.01 Pixel Detector. Computerized Med. Imag. Graph. 17:289-294
15. Harris C, Stephens MJ (1988), A combined corner and edge detector. Proc. Alvey Vision Conference 147-151
16. Brand P (1995) Reconstruction tridimensionnelle d'une scéne á partir d'une caméra en mouvement : de l'influence de la précision. PhD thesis, University Claude Bernard (Lyon I)
17. Lucas BD, Kanade T (1981), An Iterative Image Registration Technique with an Application to Stereo Vision. Proc. 7th International Joint Conference on Artificial Intelligence 674-679.
18. Luo P-F, Chao YJ, Sutton MA, Peters WH (1993) Accurate measurement of three-dimensional deformations in deformable and rigid bodies using computer vision. Exp. Mech. 33:123-132
19. Garcia D, Orteu J-J, Penazzi L (2002) A combined temporal tracking and stereo-correlation technique for accurate measurement of 3D displacements: Application to sheet metal forming. J. Mat. Proc. Tech. 125-126:736-742
20. Vic-3D. Correlated Solutions Incorporated. http://www.correlatedsolutions.com
21. ARAMIS. GOM, http://www.gom.com
22. StrainMaster. LaVision, http://www.lavision.de
23. Q-400. Dantec Dynamics. http://www.dantecdynamics.com
24. Correli STC. Holo3. http://www.holo3.com
25. Besnard G, Lagrange J-M, Hild F, Roux S, Voltz C (2010) Characterization of necking phenomena in high speed experiments by using a single camera. EURASIP J. Im. Video. Proc. 2010:215956
26. Besnard G, Hild F, Lagrange J-M, Martinuzzi P, Roux S (2012) Analysis of necking in high speed experiments by stereocorrelation. Int. J. Impact Eng. 49:179-191
27. Fusiello A (2000) Uncalibrated Euclidean reconstruction: a review. Im. vis. comput. 18:555-563
28. Kruppa E (1913) Zur Ermittlung eines Objektes aus zwei Perspektiven mit innerer Orientierung. Hölder
29. Faugeras OD, Luong QT, Maybank SJ (1992), Camera self-calibration: Theory and experiments. Proc. 2nd ECCV. Springer-Verlag
30. Faugeras O (1993) Three-dimensional computer vision: a geometric viewpoint. MIT Press, Cambridge, MA (USA)
31. Piegl L, Tiller W (1997) The NURBS Book - 2nd Edition. Springer
32. Besnard G, Hild F, Roux S (2006) “Finite-element” displacement fields analysis from digital images: Application to Portevin-Le Châtelier bands. Exp. Mech. 46:789-803
33. Roux S, Hild F, Viot P, Bernard D (2008) Three dimensional image correlation from X-Ray computed tomography of solid foam. Comp. Part A 39:1253-1265
34. Cottrell JA, Hughes TJR, Bazilevs Y (2009) Isogeometric Analysis: Toward Integration of CAD and FEA. Wiley

35. Roux S, Hild F (2006) Stress intensity factor measurements from digital image correlation: post-processing and integrated approaches. Int. J. Fract. 140:141-157

36. Dassault Systems (2008) CATIA V5 R19, Online documentation. http://www.3ds.com/products/catia/welcome/

37. Dufour J-E, Hild F, Roux S (2013) Integrated digital image correlation for the evaluation and correction of optical distortions. Submitted for publication

38. Yoneyama S, Kikuta H, Kitagawa A, Kitamura K (2006) Lens distorsion correction for digital image correlation by measuring rigid body displacement. Opt. Eng. 45:02360

39. Lava P, Van Paepegen W, Coppieters S, De Baere I, Debruyne D (2013), Impact of lens distorsions on strain measurements obtained by digital image correlation. Proc. SEM XII International Congress and Exposition on Experimental and Applied Mechanics 3:233-238

40. Jalid A, Hariri S, Senelaer J-P, El Gharad A (2009) Evaluation des incertitudes de mesure sur une machine à mesurer tridimensionnelle : Nouvelle méthode d'estimation des paramètres de surface et incertitude associées. Proc. 19^{me} Congrès Français de Mécanique, Marseille (France), 8 p.

41. Seitz SM, Curless B, Diebel J, Scharstein D, Szeliski R (2006) Proc. IEEE Conf. Computer Vision and Pattern Recognition 1:519-526

42. Vu H-H, Labatut P, Pons J-P, Keriven R (2012) High Accuracy and Visibility-Consistent Dense Multiview Stereo. IEEE Trans. Pattern Anal. Machine Intell. 34:889-901